

Validation and Parametric Investigations of an Internal Permanent Magnet Motor Using a Lumped Parameter Thermal Model

Sebastien Sequeira

Mechanical Engineering,
Georgia Institute of Technology,
Atlanta, GA 30332

Kevin Bennion

National Renewable Energy Laboratory,
Golden, CO 80401

J. Emily Cousineau

National Renewable Energy Laboratory,
Golden, CO 80401

Sreekant Narumanchi

National Renewable Energy Laboratory,
Golden, CO 80401

Gilbert Moreno

National Renewable Energy Laboratory,
Golden, CO 80401

Satish Kumar

Mechanical Engineering,
Georgia Institute of Technology,
Atlanta, GA 30332

Yogendra Joshi

Mechanical Engineering,
Georgia Institute of Technology,
Atlanta, GA 30332

One of the key challenges for the electric vehicle industry is to develop high-power-density electric motors. Achieving higher power density requires efficient heat removal from inside the motor. In order to improve thermal management, a multiphysics modeling framework that is able to accurately predict the behavior of the motor, while being computationally efficient, is essential. This paper first presents a detailed validation of a lumped parameter thermal network (LPTN) model of an Internal Permanent Magnet synchronous motor within the commercially available MOTOR-CAD modeling environment. The validation is based on temperature comparison with experimental data and with more detailed finite element analysis (FEA). All critical input parameters of the LPTN are considered in detail for each layer of the stator, especially the contact resistances between the impregnation, liner, laminations, and housing. Finally, a sensitivity analysis for each of the critical input parameters is provided. A maximum difference of 4%—for the highest temperature in the slot-winding and the end-winding—was found between the LPTN and the experimental data. Comparing the results from the LPTN and the FEA model, the maximum difference was 2% for the highest temperature in the slot-winding and end-winding. As for the LPTN sensitivity analysis, the thermal parameter with the highest sensitivity was found to be the liner-to-lamination contact resistance.

[DOI: 10.1115/1.4053121]

Keywords: electric motor, thermal management, lumped parameter network, FEA, sensitivity analysis, contact resistances, motor cooling

Introduction

Each year, the number of electric vehicles (EVs) on the road is increasing [1,2]. However, one of the main limiters to EV adoption is the range, currently lower than the range of conventional internal combustion engine vehicles. One solution to improve this range is to increase the power density of the electric motors used in the EVs. In this regard, an electric motor power density target of 50kW/L by 2025 was set by U.S. DRIVE consortium, part of the U.S. Department of Energy (DOE) [2].

For a long time, electric motors did not need to operate over a large speed range. As a result, electromagnetic optimization was set as the main solution to increase the power density of the machine and the thermal design was a secondary step, less important. However, as the operating speed range for these electric machines increased significantly once applied to vehicles, the thermal constraints due to power losses inside the motor have progressively become a limit for electromagnetic improvements. Indeed, the power losses and the generated magnetic field in an electric motor are correlated and reaching the highest performance is all about reaching the good tradeoff between the electromagnetics and heat transfer [3]. Therefore, overcoming these thermal constraints is now viewed as one of the hardest challenges to meet the ever-increasing power density objective [4,5].

This challenge requires electric machine designers to predict the temperatures of the motor for different operating modes at the

early stage of the design phase. This prediction must be accurate enough for selecting the best design solution, and fast enough for exploring the greatest number of solutions. Two modeling approaches can be used to predict the motor temperatures. The first approach is a full numerical model, usually based on a finite element analysis (FEA) [6,7] or computational fluid dynamics/heat transfer (CFD/HT) [7–9]. The second approach is the analytical model, usually employing a lumped parameter thermal network (LPTN). CFD/HT and FEA can predict the temperatures of a complex geometry with a high resolution but can have high computational costs/time [7], which is not ideal if we want to minimize the time per design iteration. Meanwhile, the LPTN has a much lower time per design iteration, but its temperature resolution is lower due to a limited number of nodes. Although the first LPTN models had a poor resolution due to a very low number of nodes, more recent densely discretized LPTN models have convinced engineers to adopt these models for the design of electric machines [7]. LPTN model validations have been demonstrated in several papers for both steady-state and transient conditions, and for different types of motors [5,10–12]. A detailed description of the resistance network for each element of the LPTN based on their geometry and material properties is provided in Ref. [7]. More recent work on LPTN models provides an even more spatially resolved discretization especially for the windings [4,13]. However, limited attention is given to parts of the motor where the material properties strongly depend on the manufacturing processes, such as the liner interface or stator to housing interface.

In this paper, we compare an LPTN model against and FEA model as well as experimental data. The hot spot of an internal permanent magnet motor is very often in the winding. Consequently, only the stator was considered in this study. Previous work on LPTN validation [11–13] through comparison with

Contributed by the Electronic and Photonic Packaging Division of ASME for publication in the JOURNAL OF ELECTRONIC PACKAGING. Manuscript received March 31, 2021; final manuscript received November 21, 2021; published online February 7, 2022. Assoc. Editor: Jaeho Lee.

This work is in part a work of the U.S. Government. ASME disclaims all interest in the U.S. Government's contributions.

Table 1 Nissan Leaf electric motor features

Feature	Value
Maximum torque (N · m)	280
Maximum power (kW)	80
Top speed (rpm)	10,390
Weight (kg)	58
Volume (m ³)	0.019
Number of poles	8
Number of stator slots	48

experimental data was focused on analyzing individual temperature points. However, this is not enough information to understand how each component contributes to the temperature rise inside the stator. Here, we propose a different approach by analyzing temperature profiles along three different paths of the motor, with particular attention to the end-windings region and the different contact interfaces in the stator.

Each thermal parameter of our LPTN is clearly investigated, and the relations between the LPTN parameters and FEA parameters are given. Moreover, the sensitivity of the main thermal parameters is computed. The thermal parameters with the highest influence on the motor increase in temperatures were identified thanks to this sensitivity analysis. We also explain how this influence is related to future motor cooling system requirements.

Experimental Data and Modeling Approach

The Nissan Leaf Electric Motor from Nissan Motor Co. Ltd. (Yokohama, Kanagawa, Japan) is our reference for all geometric, material, and thermal parameters used in this paper. The Nissan Leaf motor features are shown in Table 1 [14]. The only active cooling system is an external water jacket composed of three channels in series made of aluminum. The water jacket coolant is water-ethylene glycol.

The thermal analysis in this paper is focused on the stator where we have the highest temperature. This highest temperature is in the winding and the wire insulation deterioration caused by the high temperatures fixes the maximum temperature allowed in the stator.

The experimental results used in this study are taken from previous experiments in Ref. [15]. In these experiments, the windings were supplied with direct current (DC) current (voltage of 1.4 V and current of 165 amps) and the rotor was removed from the motor. The total heat generation from the three phases of the motor was 567 W. The only heat rejection system was the water jacket. The latter was filled with water-ethylene glycol coolant at 50% volume of water. The flow rate was 10 L/min. Thermal insulation was used to reduce natural convection from the external surfaces directly exposed to ambient air (end-windings, inner stator, housing). The boundary conditions of these experiments can be seen in Fig. 1.

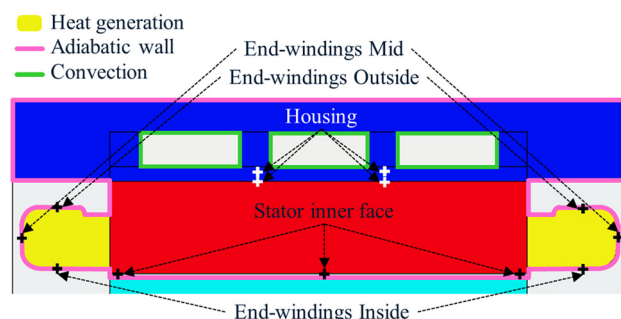


Fig. 1 Thermocouple locations on the Leaf motor stator and their associated labels, using MOTOR-CAD environment. Heat generation and boundary conditions are shown as well.

Temperatures were measured with K-type thermocouples [15]. The locations of each thermocouple are shown in Fig. 1 (black and white crosses). All temperature points in the cross-sectional plane, Fig. 1, except the *housing* temperature points, are measured in two other cross-sectional planes rotated by 120 deg and 240 deg with respect to the motor axial axis.

In this paper, we consider that a temperature label can be the same for different thermocouples or temperatures by assuming stator symmetries. A set of temperature points having the same label means they should all have the same temperature value based on the assumed symmetries in the models defined thereafter. For instance, we assume that *end-windings inside* temperature points have the same value for both rear and front end-windings. Similarly, we consider that the *stator inner face* temperature points have the same temperature along the axial length of the tooth. These assumptions are made in order to have a consistent comparison between experimental data and modeling results.

By assuming these symmetries, we end up with only five different temperatures to be compared against the models. In fact, inserting thermocouples inside the stator or the windings requires dismantling the laminations or the slot-windings, which would cause a different thermal behavior of the machine. This represents one of the main difficulties for model validation against experimental temperature values. However, in order to have a good validation of the LPTN model, we still need to know if the temperatures inside the stator and the slot-windings are consistent. Therefore, the LPTN temperature outputs are also compared to an FEA model of the complete stator. This FEA model is presented in the Finite Element Analysis Model Approach section.

Finite Element Analysis Model Approach. We used the same motor geometry and boundary conditions in the FEA model as for the experiments. The same power loss input (567 W) was used and radiation and convection with ambient air are neglected. Table 2 gives thermal conductivities for each material involved in the model, thermal contact conductance at each interface, and the water jacket's thermal properties. Thermal conductivities and conductances are estimated from the data provided in Refs. [16–18]. The water jacket's heat-transfer coefficient is derived from a CFD/HT simulation of the complete water-jacket channels in Ref. [15]. The coolant mean temperature value in the water jacket is also taken from Ref. [15]. The tests in Refs. [14] and [15] were conducted based on the Nissan Leaf motor parts. This makes the evaluation of the FEA model thermal parameters more accurate than deducing these from a different motor. We must note that the values for slot-windings-to-liner and liner-to-laminations thermal

Table 2 Thermal conductivities along each direction of a cylindrical system and thermal contact conductance used for the FEA model along with water jacket thermal properties

Thermal conductivity (W m ⁻¹ K ⁻¹)			
	Radial	Tangential	Axial
Stator laminations	21.9	21.9	1.77
Slot-windings	0.99	0.99	292
End-windings	0.76	202	101
Slot liner	0.18	0.18	0.18
Aluminum	167	167	167
Thermal contact conductance (W m ⁻² K ⁻¹)			
Slot-windings liner	1645		
Liner laminations	556		
Laminations housing	5555		
Water-jacket cooling system			
Heat transfer coefficient (W m ⁻² K ⁻¹)	1428		
Flow rate (L min ⁻¹)	10.0		
Coolant mean temperature (°C)	65		

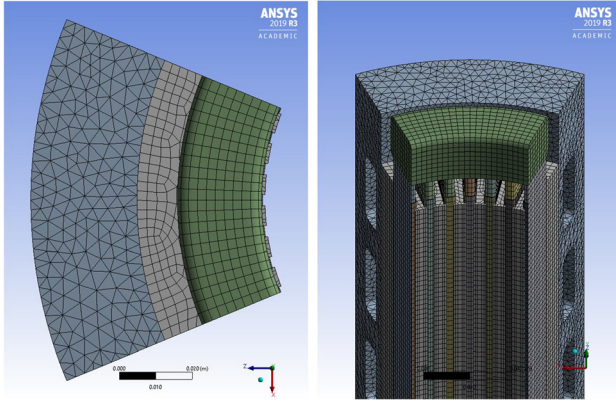


Fig. 2 Mesh of the FEA model (average size of 2.7 mm)

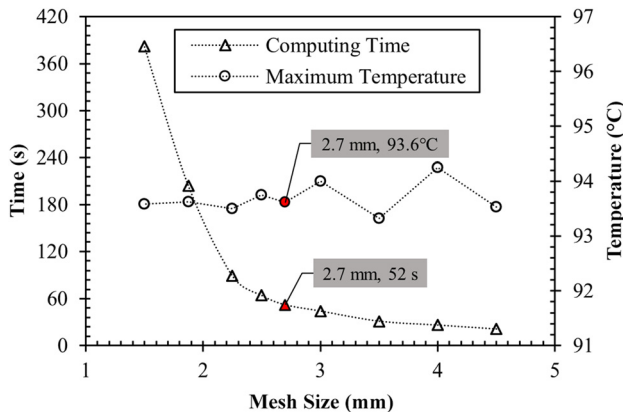


Fig. 3 Computing time and maximum temperature of the FEA model with respect to mesh size

contact conductances are not exactly the same values as those provided in Ref. [15]. Indeed, NREL provided slightly different values, which were not published yet. The liner contact conductance values are preliminary results which require further confirmation.

Two pictures of the FEA model mesh are shown in Fig. 2. The average mesh size was fixed at 2.7 mm. This choice relies on a mesh independence study. For this independence study, computing time and maximum temperature versus mesh size was computed (see Fig. 3). Red labeled markers in Fig. 3 correspond to the final average mesh size of the FEA model. With this final mesh size of 2.7 mm, the numerical results are accurate to within 0.4%.

Lumped Parameter Thermal Network Model Approach.

The LPTN model was created using MOTOR-CAD software environment, where the electric motor geometry is designed first. All

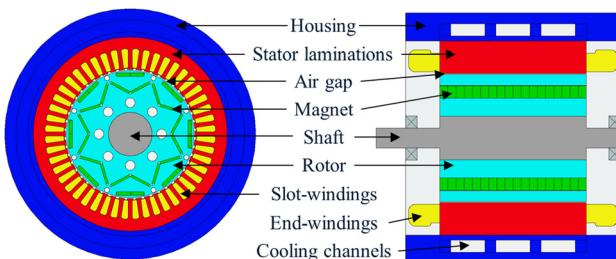


Fig. 4 Nissan Leaf motor geometry in MOTOR-CAD environment: radial cross-sectional view on the left, axial cross-sectional view on the right

dimensions from the FEA model were kept for the LPTN model. Figure 4 shows cross-sectional views of the geometry. The radial and axial views are shown on the left and right, respectively. A simplified version of the LPTN defined from this geometry is given in Fig. 5. Each colored resistance accounts for the thermal conduction through a given part of the stator. The white resistances account for thermal contact resistance at the interface between two parts of the stator. Each node of the network represents a temperature and the sources of the circuit correspond to the copper losses generated inside the windings (567 W). The LPTN main parameters are defined thereafter.

Power Loss Distribution. To be aligned with experimental results, the winding power losses are equal to the copper losses from DC currents in each phase of the stator. As we do not have AC currents in this study, we do not have any core losses or eddy current losses. As a result, the total power loss input P in the LPTN model is equal to the total electric power input from the experiments, 567 W. Besides, P is split between slot-windings and end-windings, with respect to their volume, which yields (1) and (2)

$$P_{\text{slot}} = \alpha P \quad (1)$$

$$P_{\text{end}} = \frac{1}{2}(1 - \alpha)P \quad (1)$$

$$\alpha = \frac{V_{\text{slot}}}{V_{\text{slot}} + 2V_{\text{end}}} \quad (2)$$

where V_{slot} is the total volume of slot-windings, V_{end} is the volume of each end-winding (the rear and front end-windings of the motor are considered to have the same volume), P_{slot} is the fraction of P generated inside V_{slot} , P_{end} is the fraction of P generated inside V_{end} , and α is the volume ratio between slot-windings and end-windings.

Once we know the values for P and α , P_{slot} , and P_{end} can be derived from Eqs. (1) and (2), and be integrated in the LPTN model. MOTOR-CAD does this calculation for us. Here, $\alpha = 62\%$ and $P = 567 \text{ W}$. P_{slot} and P_{end} can now be calculated which yields: $P_{\text{slot}} = 351.5 \text{ W}$ and $P_{\text{end}} = 107.7 \text{ W}$.

Stator Lamination Thermal Conductivity. The stator stack is made of silicon steel sheets (also called electrical steel) separated by a thin layer of coating material called the interlamination layer. In fact, this coating layer is not an independent material but is created when the silicon steel sheet is treated. Consequently, the equivalent thermal conductivity k_{int} of this inert-lamination layer is hard to predict [16]. To overcome this issue, k_{int} was defined as

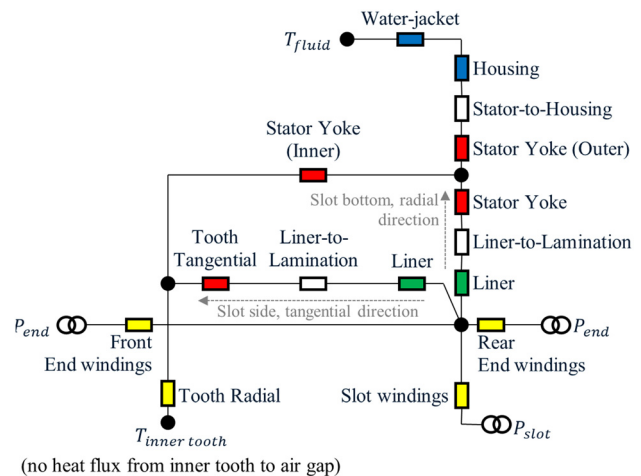


Fig. 5 Simplified representation of the stator LPTN model (based on MOTOR-CAD schematic)

a function of stator stack equivalent thermal conductivities (see values Table 2), and silicon steel thermal conductivity k_{steel} . These thermal conductivities are much easier to measure than k_{int} . In the following paragraph, we show how the relations between the different thermal conductivities were derived.

The successive silicon steel and interlamination layers of the stator stack can be seen in Fig. 6. The laminations are positioned in (X, Y) plane normal to the axial direction of the motor $(Z\text{-axis in Fig. 6})$. The individual thermal resistance of each layer is a function of thickness, area of the surface normal to the heat flow direction and the thermal conductivity of the material. As we are considering the heat flow along each axis, we will have different resistance values of the same layer for a different axis. Indeed, the area and thickness along two different axes can change. Based on the notations used in Fig. 6, thermal resistances are defined as

$$X \rightarrow R_{\text{steel}X} = \frac{l}{k_{\text{steel}}A_{\text{steel}X}}, \quad R_{\text{int}X} = \frac{l}{k_{\text{int}}A_{\text{int}X}} \quad (3)$$

$$Z \rightarrow R_{\text{steel}Z} = \frac{e_{\text{steel}}}{k_{\text{steel}}A_Z}, \quad R_{\text{int}Z} = \frac{e_{\text{int}}}{k_{\text{int}}A_Z} \quad (4)$$

where $R_{\text{steel}X}$, $R_{\text{steel}Z}$, $A_{\text{steel}X}$, and A_Z are the steel sheet resistances and cross-sectional areas normal to the X and Z axes, respectively, and $R_{\text{int}X}$, $R_{\text{int}Z}$, and $A_{\text{int}X}$ are interlamination resistances and cross-sectional areas normal to the X and Z axes, respectively. One can note that the Y direction is not considered here as the resistance definition the same as for the X direction due to inherent symmetry.

Two other useful dimensions must be defined

$$A_X = nA_{\text{steel}X} + (n-1)A_{\text{int}X} \quad (5)$$

$$L = ne_{\text{steel}} + (n-1)e_{\text{int}} \quad (6)$$

where A_X is the total cross-sectional area of the stator stack normal to X -axis, L is the total length of the stator stack along Z -axis, and n is the total number of silicon steel sheets.

Along the X direction, thermal resistances between each layer are in parallel whereas along the Z direction, thermal resistances are in series, as drawn in Fig. 6. This observation yields Eqs. (7) and (8), which define the stator stack equivalent thermal resistances R_X and R_Z , respectively,

$$\frac{1}{R_X} = \frac{n}{R_{\text{steel}X}} + \frac{n-1}{R_{\text{int}X}} \quad (7)$$

$$R_Z = nR_{\text{steel}Z} + (n-1)R_{\text{int}Z} \quad (8)$$

Stator stack equivalent thermal conductivities k_X (along X -axis) and k_Z (along Z -axis) can be expressed as a function of R_X and R_Z , respectively,

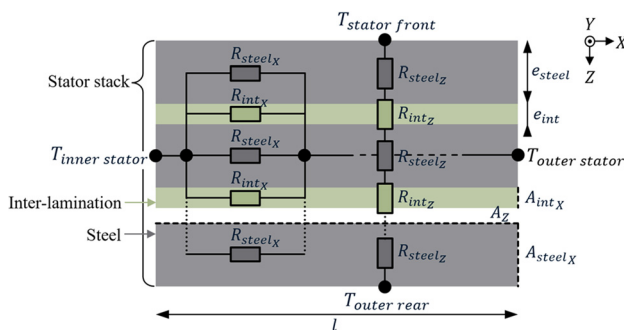


Fig. 6 Stator laminations cross-sectional view. Z -axis corresponds to the stator axial axis.

$$k_X = \frac{l}{R_X A_X} \quad (9)$$

$$\frac{1}{k_Z} = \frac{R_Z A_Z}{L} \quad (10)$$

The stacking factor S_f is defined as the ratio of cross-sectional area of silicon steel to the overall cross-sectional area of stator laminations. We can use our notations from Fig. 6 to come up with the expression of S_f as follows:

$$S_f = \frac{nA_{\text{steel}X}}{A_X} = \frac{ne_{\text{steel}}}{L} \quad (11)$$

For the Nissan Leaf electric motor stator, $S_f = 0.97$ [19]. Combining Eqs. (3), (5), (7), (9), and (11) yields Eq. (12) and combining Eqs. (4), (6), (8), (10), (11) yields Eq. (13) given below. Again, inherent symmetries imply $k_X = k_Y$

$$k_X = k_Y = S_f \times k_{\text{steel}} + (1 - S_f) \times k_{\text{int}} \quad (12)$$

$$\frac{1}{k_Z} = \frac{S_f}{k_{\text{steel}}} + \frac{1 - S_f}{k_{\text{int}}} \quad (13)$$

In MOTOR-CAD, k_{steel} , and k_{int} are used as input values. k_{steel} and k_{int} are derived from Eqs. (12) and (13) with respect to k_X , k_Y , and k_Z values. In order to have a fair comparison with the FEA model, k_X , k_Y , and k_Z values are taken from Table 2. Solving Eqs. (12) and (13) for k_{int} and k_{steel} , we have the thermal conductivity input values for our LPTN

$$\begin{cases} k_{\text{int}} = 0.054 \text{ W m}^{-1} \text{ }^\circ\text{C}^{-1} \\ k_{\text{steel}} = 23 \text{ W m}^{-1} \text{ }^\circ\text{C}^{-1} \end{cases}$$

Slot-Windings Equivalent Thermal Conductivity. The copper wires used for the windings have a diameter $D_c = 0.800$ mm and a total diameter (including insulation) $D = 0.885$ mm. Maximizing the number of wires, which can fit inside a single slot of the Leaf motor, leads to a maximum copper slot fill of 52%.

In the LPTN, the slot-windings are represented as a set of cuboids. The cuboid material includes the copper from the wire, the wire insulation, and the impregnation material. One cuboid contour is highlighted in Fig. 7(b). One can notice that each cuboid can have a different height or width. However, they all have the same axial length equal to the length of the active windings which is also the length of the stator. Using cuboids instead of individual wires allows to have a much faster model. Moreover, this cuboid model is not affected by the randomness of the wire distribution in the slot. The cuboid nodes are represented in Fig. 7(a). The center node temperature is equal to the average

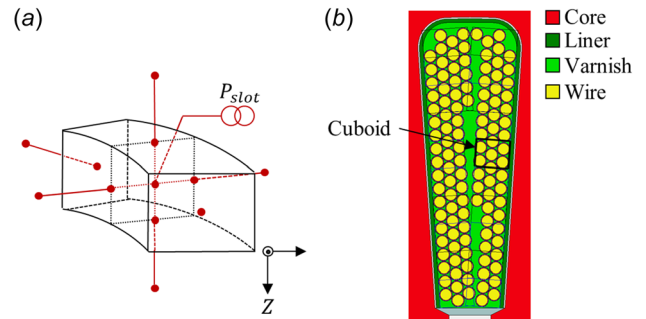


Fig. 7 Slot-windings cuboids: (a) three-dimensional model representation and (b) in-plane representation within MOTOR-CAD environment

temperature T_C of the cuboid. On node is then associated with each external face of the cuboid. Each of these nodes is connected to the rest of the LPTN. The face nodes are also connected to the central node by resistances to model the heat flow from the center of the cuboid to each of its faces (these resistances are not represented here). Copper losses are represented by a heat source located at the central node T_C . Our LPTN is composed of ten cuboids. This set of ten cuboids is represented by a single yellow resistor labeled *slot winding* on Fig. 5. The number of cuboids was decided based on a convergence study. The authors have been looking at the maximum winding temperature with respect to the number of cuboids. As shown in Fig. 8, after six cuboids, one can observe the oscillating scheme with a maximum temperature variation of $\pm 0.1^\circ\text{C}$ around the mean temperature. As $\pm 0.1^\circ\text{C}$ range is the typical measurement uncertainty of k -type thermocouples, this variation was considered as acceptable. Therefore, the authors could have chosen six cuboids instead of ten but they decided to consider the number of cuboids corresponding to the first high temperature peak in the oscillating region (worst-case scenario).

The internal resistance values between the face nodes and the center node are calculated from the equivalent thermal conductivities of the wire and impregnation material along each axis. In order to have a good comparison of LPTN results with the FEA results, we used user-defined equivalent thermal conductivities from the FEA given in Table 2. This cuboid model has already been widely used as some recent electric thermal studies show it [4,13].

End-Windings Equivalent Thermal Conductivity. End-windings are modeled as a single toroid. The thermal resistance at the interface between each end-turns and the end-winding shape irregularities are therefore not considered. As for the slot-winding, end-winding are modeled by ten cuboids connected to the slot-winding cuboids on $T_{z\pm}$ nodes. As a significant portion of a single wire in the end-winding is oriented along the tangential direction, the thermal conductivity along this tangential direction is significantly increased compared to the slot-winding thermal conductivity along the same direction. However, the thermal conductivity along the axial direction is decrease. This observation explains the different thermal conductivity values given in Table 2. As FEA and LPTN models must be accurately compared, user-defined values of end-winding thermal conductivities (taken from Table 2) were used inside MOTOR-CAD.

Stator-to-Housing Thermal Conductance. Thermal contact resistances are the most critical parameters in the LPTN model, as they are the main source of error due to manufacturing process uncertainties [3]. For example, the stator external surface roughness has a significant impact on the effective thermal contact conductance between the lamination stack and the housing [17].

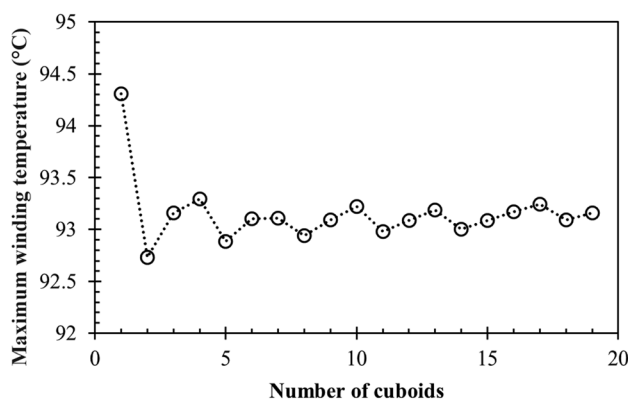


Fig. 8 Maximum winding temperature with respect to the number of cuboids (computed from thermal steady-state simulation using the LPTN)

Usually, a stator-to-housing air gap is used to account for the surface roughness. An air gap value for a good contact at the lamination-housing interface is around around 0.01 mm [20]. If we convert this air gap into an equivalent thermal contact conductance, we obtain a stator-to-housing conductance of $3171 \text{ W m}^{-2} \text{ }^\circ\text{C}^{-1}$ for the leaf motor.

In our case, the thermal conductance is $5555 \text{ W m}^{-2} \text{ }^\circ\text{C}^{-1}$ from Table 2. This thermal conductance corresponds to a mean gap of 0.006 mm. This suggests that the stator-to-housing contact conductance of the Nissan Leaf motor is better than usual good contact values from Ref. [20]. Nevertheless, this suggestion must be used carefully, as the value from the FEA model in Table 2 was derived from a temperature measurement based on a sample of the stator laminations, and not directly on the motor [17]. As this value was still consistent and as we wanted the same values between the FEA and LPTN, we kept the conductance value from Table 2.

Slot-Liner Contact. Slot-liner contact resistance is the contact between winding (in fact, the impregnation material overlaying the winding) and stator laminations. The thermal resistance is due to several manufacturing and assembly processes, which yield imperfections, along with high uncertainties in the measured value of this resistance [21]. The accurate prediction of the thermal contact resistance has been proven to be highly critical in the prediction of the machine thermal behavior [20,21].

In the real motor assembly, we have a contact conductance for the winding side of the liner $G_{\text{Liner-Wdg}}$ and a contact conductance for the lamination side of the liner $G_{\text{Liner-Lam}}$. An equivalent thermal contact conductance of the liner G_{Liner} can be defined from $G_{\text{Liner-Wdg}}$ and $G_{\text{Liner-Lam}}$

$$G_{\text{Liner}} = \left(\frac{1}{G_{\text{Liner-Lam}}} + \frac{1}{G_{\text{Liner-Wdg}}} \right)^{-1} \quad (14)$$

In MOTOR-CAD, the contact resistance derived from G_{Liner} is represented by an equivalent gap of thickness l_{gap} between the liner and the laminations filled with a mixture of impregnation material of thermal conductivity k_{imp} and air of thermal conductivity k_{air} . Indeed, the winding impregnation manufacturing process is not perfect, and tiny air pocket gets trapped in the varnish. The equivalent thermal conductivity k_{gap} of the air/varnish mixture in the gap is defined as

$$k_{\text{gap}} = f_G \times k_{\text{imp}} + (1 - f_G) \times k_{\text{air}} \quad (15)$$

where f_G is the goodness factor, ranging from 0 to 1. For a perfect contact (no air pockets), $f_G = 1$. The role of this goodness factor is to enhance or degrade the contact resistance between the liner and the impregnation by adjusting k_{gap} .

To have the correct thermal contact resistance value in the LPTN, $k_{\text{gap}}/l_{\text{gap}}$ must be equal to G_{Liner} . G_{Liner} is derived from experimental values of $G_{\text{Liner-Lam}}$ and $G_{\text{Liner-Wdg}}$ according to Eq. (14). Both k_{gap} and f_G can be adjusted to have $k_{\text{gap}}/l_{\text{gap}} = G_{\text{Liner}}$. For this work, l_{gap} was fixed to 0.1 mm based on other equivalent contact gap in MOTOR-CAD software (no specific reference was used to estimate what this thickness should be as the only important value is the resistance). As l_{gap} is fixed, k_{gap} must be equal to $G_{\text{Liner}} \times l_{\text{gap}}$. The goodness factor can then be calculated using Eq. (15). We found a value of 0.051 for f_G . The very low value of this goodness factor shows that considering a perfect contact with the liner is questionable if an accurate LPTN is needed.

They may be several explanations for low thermal contact conductance at the liner interface. First, the roughness of the lamination stack surface and liner surface could increase the mean gap between these surfaces and, therefore, increase the resistance. Second, due to a relatively high viscosity of the varnish during winding impregnation process, they may be stuck air bubbles between the winding and the liner, further deteriorating the contact goodness. Third, there is no additional pressure on the liner

that would improve the effective contact area with the laminations or the windings.

In Fig. 5, two resistors are associated with the liner-to-lamination contact resistance: one is for the contact with tooth slot side and the other is for the contact with slot bottom.

Results and Discussion

In the first part of this section, the FEA and LPTN temperature results are shown and discussed. In the second part, the results from the LPTN resistance sensitivity analysis are presented.

Lumped Parameter Thermal Network Model and Experimental Data. The comparison between experimental temperatures and LPTN temperatures is shown on the graph in Fig. 9. The labels in this figure refer to the labels from Fig. 1. The same reference temperature of 65 °C (coolant mean temperature) is used for both LPTN and experiments. As a reminder from Fig. 1, one experimental temperature value is the average of temperature measurements from different location, assuming stator symmetries. The standard deviation of these temperature measurements is computed and plot in Fig. 9 as error bars. The standard deviation of end-winding temperatures is higher than the standard deviation of the housing or the stator inner face temperatures. This higher standard deviation comes from the end-winding simplified model. Indeed, the symmetry assumption along the tangential direction is questionable as the end-windings have a more complex shape than a single toroid. Each phase end-turn has a different shape, and the wires do not have the exact same bending curve from one slot to another. Moreover, there may be some air pockets between wires. For all these reasons, each end-turn is different and creates higher deviation in the temperature measurements.

The relative error between LPTN and experiments was computed for each temperature. End-windings suffer from the highest relative error. Again, defining end-windings as a single toroid is an important simplification. Each wire is curved to go from one slot to another and create a loop, which makes the thermal conductivity of end-windings highly position-dependent. As a result, considering a fixed thermal conductivity along each axis of a cylindrical coordinate system in a single toroid is a strong simplification compared to real end-windings. Despite these simplifications, the maximum relative error between experiments and LPTN is 3.6%, which shows a satisfactory agreement between experimental results and LPTN output. Accordingly, the LPTN can accurately predict the steady-state temperatures of the Nissan Leaf motor.

Lumped Parameter Thermal Network Model and Finite Element Analysis Model. The results from the FEA steady-state thermal simulation are shown in Fig. 10. LPTN and FEA results

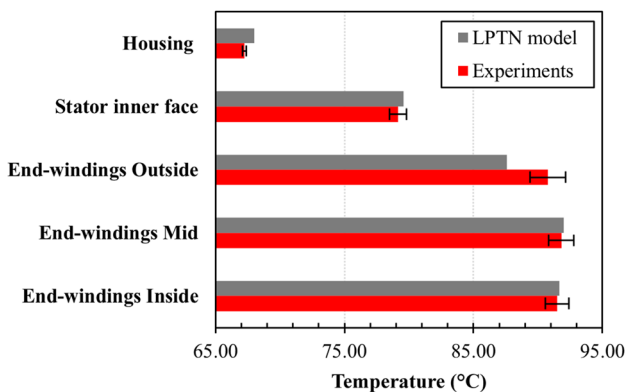


Fig. 9 Experimental temperatures versus LPTN temperatures at five different stator locations. Coolant mean temperature fixed at 65 °C for both LPTN and experiments.

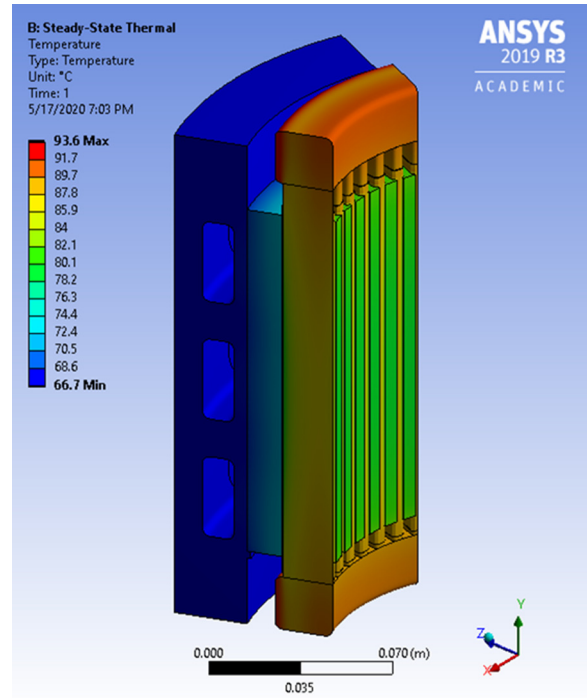


Fig. 10 Temperature results from FEA steady-state thermal simulation using ANSYS software

were compared along three different paths in the stator. These paths are represented by a dashed arrow in Fig. 11. Path (1) is colinear with the centerline of the slot-winding. It starts at the inner side of the slot and stops at the channel wall of the water jacket. Path (2) is colinear with the centerline of the tooth. It starts at the inner side of the tooth and stops at the channel wall of the water jacket. Path (3) crosses the midplane of the end-windings along the radial direction. It starts at the inner surface of the end-winding and stops at the outer surface of the same end-winding.

The FEA and LPTN temperature results along these paths are shown in Fig. 12 for path (1), Fig. 13 for path (2) and Fig. 14 for path (3). The experimental temperatures are also added to the plots in Figs. 12–14. The LPTN temperatures correspond to the node temperature in the resistance network. For Figs. 12 and 14, the cuboid temperature node, which was used for the plots is T_c (see Fig. 7), namely, the average temperature of the cuboid. In order to have an idea of the temperature extremum for each cuboid, the maximum and minimum temperatures of each cuboid were plotted as gray dotted lines on both Figs. 12 and 14. These envelopes are valid for the cuboid model only, which is only used for winding. Consequently, the dotted line is plotted only for the slot-windings part on Fig. 12. Looking at the domain between these two envelopes is more relevant when comparing the LPTN model to experimental data or FEA model since the plot of T_c temperature does not correspond necessarily to the exact same temperature point in the FEA model or in the experiments.

The maximum relative error between LPTN and FEA models for each path is given in Table 3. The overall maximum relative error is about 2%. Thus, the LPTN temperatures show an excellent agreement with the FEA temperatures for thermally critical areas in the motor, namely, the slot-windings and end-windings. From these results, one can state that an LPTN model can replace an FEA model for steady-state thermal analysis of an electric machine. The computational time for the LPTN steady-state analysis is about 4 s, whereas the FEA computational time, with the same computer configuration, is about 52 s, which makes the LPTN 13 times faster. In return, the LPTN nodal network provides coarser temperature resolution than the FEA model.

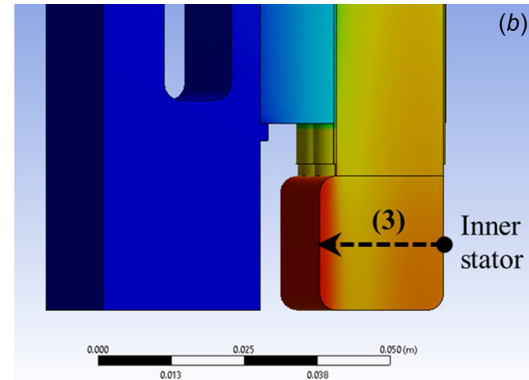
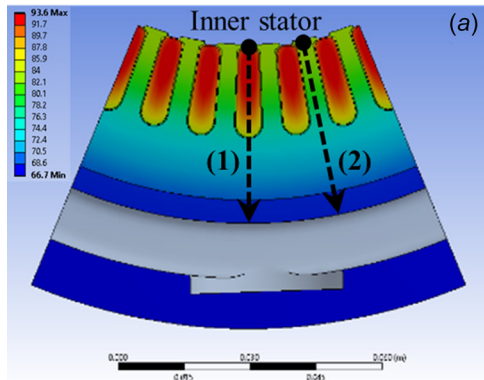


Fig. 11 Temperature profile paths: (a) path (1) and path (2) locations in the midplane cross-sectional view of the stator and (b) path (3) location in the axial cross-sectional view of the stator

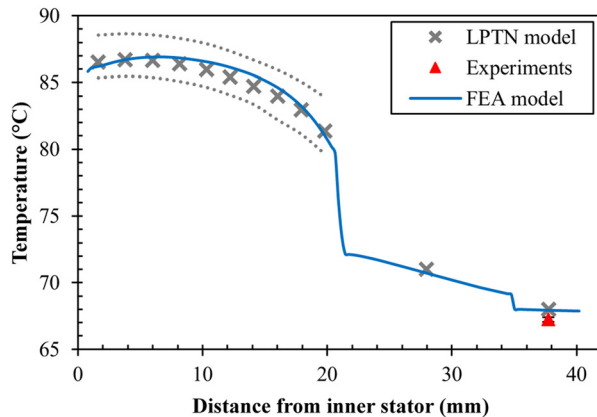


Fig. 12 Temperature profiles along a slot following path (1). Profiles are given for the FEA model, LPTN model and experimental data.

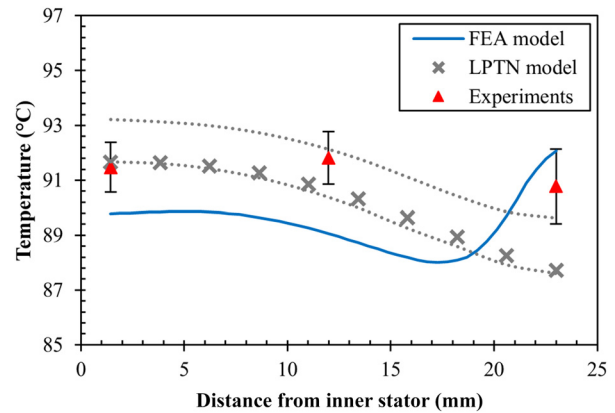


Fig. 14 Temperature profiles along end-windings following path (3). Profiles are given for the FEA model, LPTN model and experimental data.

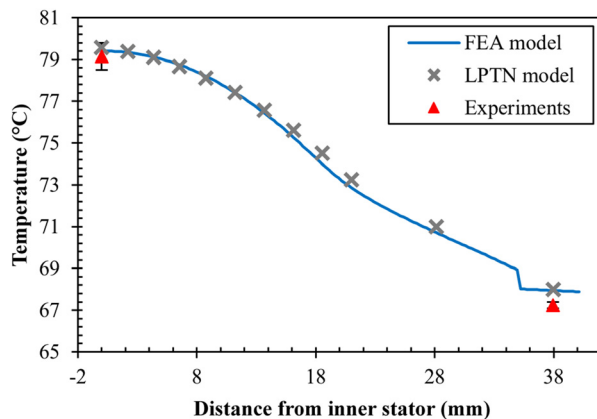


Fig. 13 Temperature profiles along a tooth following path (2). Profiles are given for the FEA model, LPTN model and experimental data.

Nevertheless, the thermal design of an electric motor is mainly focused on the highest temperature points. Indeed, for the stator, the temperature limit only comes from the winding rating. The winding temperature must be kept under a critical temperature to prevent the wire insulation deterioration. This critical temperature is given by the wire insulation class standard. As a result, having a high number of temperature points is not essential as long as the maximum temperature values in each part are accurately predicted.

Table 3 Maximum relative error between FEA and LPTN model temperature profiles

Path	Error
(1) → Slot-windings	0.95%
(2) → Stator tooth	0.52%
(3) → End-windings	2.08%

The lowest error is found along path (2). This path only crosses the stator laminations and the housing. Stator laminations are composed of evenly distributed silicon iron sheets perpendicular to the axial direction of the stator. In this case, the thermal conductivities are well known and the resistance values in the LPTN can be computed with a low uncertainty, hence the low error along path (2). The highest error is in the end-windings (Fig. 14). We have already discussed about the uncertainty in the end-windings due to its simplified toroid model in LPTN Model and Experimental Data section. The FEA model also uses a single toroid with a fixed orthotropic thermal conductivity; however, the LPTN and FEA temperature profiles are reversed in the region beyond 17 mm from the inner stator.

The reason for this temperature rise in the FEA model comes from the low radial thermal conductivity value compared to the axial, and tangential thermal conductivities in the end-windings, see Table 2. To give a more detailed explanation, the end-winding toroid volume is represented as a combination of two volumes \mathcal{V}_1 and \mathcal{V}_2 as shown in Fig. 15. \mathcal{V}_2 is the volume beyond 17 mm from the inner stator surface. In Fig. 15, the heat flux q_2 from \mathcal{V}_2 to \mathcal{V}_1 flows along the radial direction and, unlike \mathcal{V}_1 , \mathcal{V}_2 is not directly

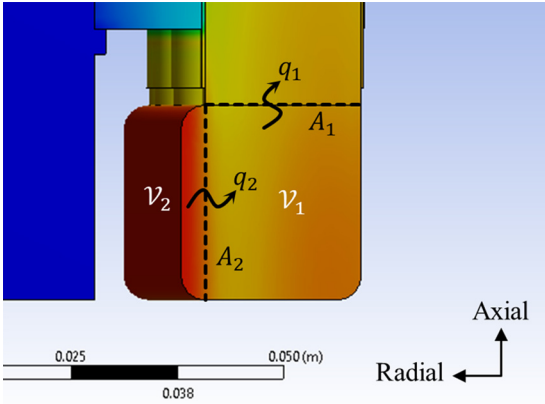


Fig. 15 End-windings heat flux and volume separation

connected to the slot-windings. As a result, the heat produced in \mathcal{V}_2 leaves through surface A_2 (convection is neglected). Yet, the thermal conductivity along the radial direction is much lower than that along the axial direction—direction of the heat flux q_1 from \mathcal{V}_1 to the slot-windings. This results in a temperature increase in \mathcal{V}_2 away from A_2 in the radial direction, hence, the jump in temperature for the FEA model, Fig. 14. In the LPTN this jump does not exist. Indeed, end-windings are represented as a set of cuboids in the LPTN model and each cuboid is connected to the slot-winding cuboids on their $T_{z\pm}$ nodes (see Fig. 7). This means all cuboids from the end-windings are directly connected to the slot-winding cuboids, and thus, there is no equivalent volume \mathcal{V}_2 , as for the FEA, which is not directly connected to the end-windings. This explains why LPTN temperature profile is still decreasing as we go beyond the bottom of the slot-winding.

Eventually, in Fig. 14, the LPTN predictions are closer to the experiments. This is consistent as, in the real motor, all wires come from the slot-windings and there is no equivalent side volume \mathcal{V}_2 disconnected from the rest of the windings.

Sensitivity Analysis. A sensitivity analysis using the LPTN model can help identify the most critical resistances rise in the stator [22]. Usually, for a sensitivity analysis, the thermophysical properties of the different materials are considered [23]. However, because both thermal conductances and thermal conductivities are considered in this study, the present sensitivity analysis is based on their equivalent thermal resistance. The final thermal parameters and their associated thermal resistance names chosen for our sensitivity analysis are given in Table 4.

The LPTN used for the sensitivity analysis was based on a 20% and 50% value reduction for each thermal resistance in Table 4. The sensitivity was defined as the temperature difference ΔT between the winding maximum temperature with initial resistances and the winding maximum temperature with the new reduced resistance. Figure 16 shows the sensitivity analysis ΔT output for each resistance and each percentage reduction. Figure 16 shows that the *liner contact* resistance has the highest influence on the temperature variation of the motor, followed by the *liner*

Table 4 List of thermal resistances used for the sensitivity analysis, and their related initial thermal parameter

Thermal resistance	Associated thermal parameter
R [liner contact]	Liner-to-lamination thermal contact conductance
R [liner]	Liner thermal conductivity
R [slot-windings]	Slot-windings equivalent thermal conductivity
R [water-jacket]	Channels heat transfer coefficient
R [housing contact]	Housing-to-lamination thermal contact conductance
R [housing]	Housing thermal conductivity

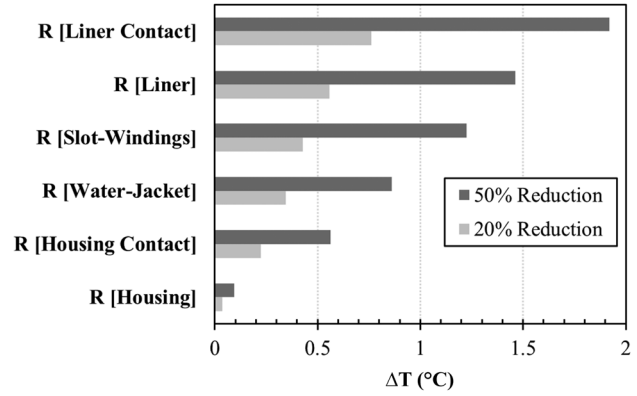


Fig. 16 Sensitivity analysis of the LPTN thermal resistances for 20% and 50% value reductions

resistance. This high influence of the liner relates to the highest temperature decrease ($\approx 7^\circ\text{C}$), at 21 mm from the inner stator in Fig. 12. This temperature decrease occurs along a very short distance, less than 1 mm, corresponding to the liner area.

The liner influence is due to the low thermal conductivity of the liner compared to other thermal conductivities involved (see Table 2). Also, this influence comes from the low contact thermal conductance of the liner compared to other thermal conductances like the stator-to-housing contact conductance. Although the difference between contact thermal conductances of the liner compared to other conductances seems quite high, it remains consistent. Indeed, stator-to-housing thermal resistance is essentially caused by laminations roughness. At the lamination-to-liner interface, this same roughness is responsible for a decrease in the contact conductance. However, imperfections during impregnation process, as well as remaining air between the liner and the laminations significantly impact further reduction of the liner contact conductance.

It is worth noticing that *water-jacket* resistance sensitivity is less than half of the liner contact resistance sensitivity. This shows that improving the heat transfer coefficient of a cooling jacket system outside of the slot-windings has some limitations in terms of maximum temperature reduction. This is particularly illustrated in Fig. 17. The limitation of increasing the heat transfer coefficient is represented by the dashed line asymptote equal to 91.50°C . Therefore, the maximum temperature difference between the current heat transfer coefficient ($1428 \text{ W m}^{-2} \text{ }^\circ\text{C}^{-1}$) and an infinite heat transfer coefficient is about 1.7°C .

From the previous observations, we can draw an important conclusion. The next-generation cooling systems that will make

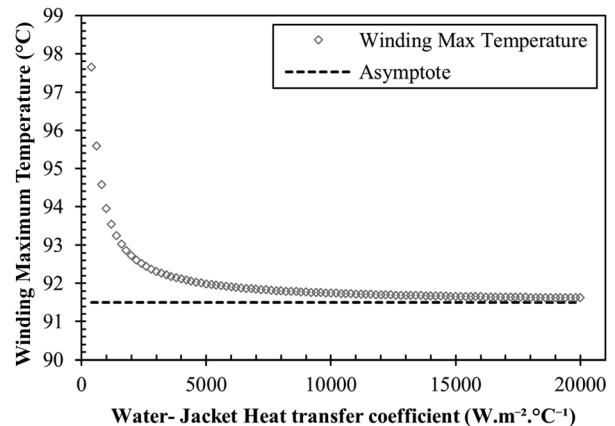


Fig. 17 Winding maximum temperature as a function of water jacket's heat transfer coefficient. Results are computed with our LPTN model.

internal permanent magnet motors reach high power densities must be between the liner and the windings. According to the sensitivity analysis, improving the water jacket's heat transfer coefficient or the stator-to-housing conductance will not provide enough temperature decrease in the windings. Thus, creating direct cooling of the windings with a focus on end-windings, as end-windings are subject to the maximum temperature, seems inevitable for reaching significantly higher power densities.

Conclusions

In this paper, we have first proposed a detailed comparison of an LPTN model with experimental data for steady-state thermal analysis of the Nissan Leaf motor stator. The maximum temperature difference between LPTN and experimental temperatures was under 4%. The LPTN model was also compared to an FEA model, with a maximum difference of 2%. End-windings were found to be a critical region in terms of modeling accuracy. Temperature profile differences have been explained in detail, especially for the end-windings outside region extending beyond the bottom of the slots.

Consequently, as LPTN accuracy can get very close to FEA model accuracy, LPTN can potentially replace FEA models during the design phase. This is particularly interesting when a high number of multiphysics transient simulations (combining thermal, electromagnetic, and mechanical models) are required to compare multiple motor configurations during the design process. Indeed, transient simulations of electric machines can be very important, especially for EV applications, due to the high number of transient modes in drive cycles.

Finally, a sensitivity analysis was conducted for six thermal resistances involved in the LPTN model. Liner contact resistance had the highest influence. Comparing influences of other thermal resistances shows that improving heat transfer coefficient of a cooling system outside of the stator does not provide significant temperature reduction of the windings. Creating a very high-power-density electric motor will require having a cooling system inserted between the liner and the winding.

Acknowledgment

This material is based upon work supported by the U.S. Department of Energy's Office of Energy Efficiency and Renewable Energy (EERE) under the Vehicle Technologies Program Office Award Number DE-EE0008708. The authors would like to particularly acknowledge Amitav Tikadar for help with LPTN modeling within MOTOR-CAD environment.

This work was authored in part by the National Renewable Energy Laboratory (NREL), operated by Alliance for Sustainable Energy, LLC, for the U.S. Department of Energy (DOE) under Contract No. DE-AC36-08GO28308. Funding was provided by the DOE Vehicle Technologies Office. The views expressed in the article do not necessarily represent the views of the DOE or the U.S. Government.

This report was prepared as an account of work sponsored by an agency of the U.S. Government. Neither the U.S. Government nor any agency thereof, nor any of their employees, makes any warranty, express or implied, or assumes any legal liability or responsibility for the accuracy, completeness, or usefulness of any information, apparatus, product, or process disclosed, or represents that its use would not infringe privately owned rights. Reference herein to any specific commercial product, process, or service by trade name, trademark, manufacturer, or otherwise does not necessarily constitute or imply its endorsement, recommendation, or favoring by the U.S. Government or any agency thereof.

Funding Data

- U.S. Department of Energy's Office of Energy Efficiency and Renewable Energy (EERE) under the Vehicle

Technologies Program Office (Award No. DE-EE0008708; Funder ID: 10.13039/100006134).

- National Renewable Energy Laboratory (NREL), operated by Alliance for Sustainable Energy, LLC, for the U.S. Department of Energy (DOE) (Contract No. DE-AC36-08GO28308).

References

- [1] I. E. A. (IEA), 2019, *Global EV Outlook 2019*, IEA, Paris, France.
- [2] Office of Energy Efficiency & Renewable Energy, 2017, "Electrical and Electronics Technical Team Roadmap," U.S. Driving Research and Innovation for Vehicle Efficiency and Energy Sustainability, Washington, DC.
- [3] Staton, D., Boglietti, A., and Cavagnino, A., 2005, "Solving the More Difficult Aspects of Electric Motor Thermal Analysis in Small and Medium Size Industrial Induction Motors," *IEEE Trans. Energy Convers.*, **20**(3), pp. 620–628.
- [4] Madonna, V., Walker, A., Giangrande, P., Serra, G., Gerada, C., and Galea, M., 2019, "Improved Thermal Management and Analysis for Stator End-Windings of Electrical Machines," *IEEE Trans. Ind. Electron.*, **66**(7), pp. 5057–5069.
- [5] Popescu, M., Staton, D. A., Boglietti, A., Cavagnino, A., Hawkins, D., and Goss, J., 2016, "Modern Heat Extraction Systems for Power Traction Machines—A Review," *IEEE Trans. Ind. Appl.*, **52**(3), pp. 2167–2175.
- [6] Lu, Q., Zhang, X., Chen, Y., Huang, X., Ye, Y., and Zhu, Z. Q., 2015, "Modeling and Investigation of Thermal Characteristics of a Water-Cooled Permanent-Magnet Linear Motor," *IEEE Trans. Ind. Appl.*, **51**(3), pp. 2086–2096.
- [7] Boglietti, A., Cavagnino, A., Staton, D., Shanel, M., Mueller, M., and Mejuto, C., 2009, "Evolution and Modern Approaches for Thermal Analysis of Electrical Machines," *IEEE Trans. Ind. Electron.*, **56**(3), pp. 871–882.
- [8] Fan, X., Zhang, B., Qu, R., Li, D., Li, J., and Huo, Y., 2019, "Comparative Thermal Analysis of IPMSMs With Integral-Slot Distributed-Winding (ISDW) and Fractional-Slot Concentrated-Winding (FSCW) for Electric Vehicle Application," *IEEE Trans. Ind. Appl.*, **55**(4), pp. 3577–3588.
- [9] Lindh, P., Petrov, I., Jaatinen-Vari, A., Gronman, A., Martinez-Iturralde, M., Satrustegui, M., and Pyrhonen, J., 2017, "Direct Liquid Cooling Method Verified With an Axial-Flux Permanent-Magnet Traction Machine Prototype," *IEEE Trans. Ind. Electron.*, **64**(8), pp. 6086–6095.
- [10] Chen, Q., Zou, Z., and Cao, B., 2017, "Lumped-Parameter Thermal Network Model and Experimental Research of Interior Pmsm for Electric Vehicle," *CES Trans. Electr. Mach. Syst.*, **1**(4), pp. 367–374.
- [11] Mellor, P. H., Roberts, D., and Turner, D. R., 1991, "Lumped Parameter Thermal Model for Electrical Machines of TEFC Design," *IEE Proc. B Electric Power Appl.*, **138**(5), pp. 205–218.
- [12] Refaie, A. M. E., Harris, N. C., Jahns, T. M., and Rahman, K. M., 2004, "Thermal Analysis of Multibarrier Interior PM Synchronous Machine Using Lumped Parameter Model," *IEEE Trans. Energy Convers.*, **19**(2), pp. 303–309.
- [13] Zhang, H., Giangrande, P., Sala, G., Xu, Z., Hua, W., Madonna, V., Gerada, D., and Gerada, C., 2021, "Thermal Model Approach to Multisector Three-Phase Electrical Machines," *IEEE Trans. Ind. Electron.*, **68**(4), p. 2919.
- [14] Sato, Y., Ishikawa, S., Okubo, T., Abe, M., and Tamai, K., 2011, "Development of High Response Motor and Inverter System for the Nissan LEAF Electric Vehicle," *SAE Technical Paper No. 2011-01-0350*.
- [15] Moreno, G., 2016, "Thermal Performance Benchmarking: Annual Report," National Renewable Energy Lab. (NREL), Golden, CO, Report No. NREL/MP-5400-64941.
- [16] Cousineau, J. E., Bennion, K., DeVoto, D., and Narumanchi, S., 2019, "Experimental Characterization and Modeling of Thermal Resistance of Electric Machine Lamination Stacks," *Int. J. Heat Mass Transfer*, **129**, pp. 152–159.
- [17] Emily Cousineau, J., Bennion, K., Chieduko, V., Lall, R., and Gilbert, A., 2018, "Experimental Characterization and Modeling of Thermal Contact Resistance of Electric Machine Stator-to-Cooling Jacket Interface Under Interference Fit Loading," *ASME J. Therm. Sci. Eng. Appl.*, **10**(4), p. 041016.
- [18] Wereszczak, A. A., Emily Cousineau, J., Bennion, K., Wang, H., Wiles, R. H., Burress, T. B., and Wu, T., 2017, "Anisotropic Thermal Response of Packed Copper Wire," *ASME J. Therm. Sci. Eng. Appl.*, **9**(4), p. 041006.
- [19] Motor Design Ltd., 2019, "Modelling the Nissan Leaf Motor Using Motor-CAD," Motor Design Ltd., Wrexham, UK, accessed Mar. 29, 2019, <https://www.motor-design.com/resources/>
- [20] Boglietti, A., Cavagnino, A., and Staton, D., 2008, "Determination of Critical Parameters in Electrical Machine Thermal Models," *IEEE Trans. Ind. Appl.*, **44**(4), pp. 1150–1159.
- [21] Wrobel, R., Williamson, S. J., Booker, J. D., and Mellor, P. H., 2016, "Characterizing the in Situ Thermal Behavior of Selected Electrical Machine Insulation and Impregnation Materials," *IEEE Trans. Ind. Appl.*, **52**(6), pp. 4678–4687.
- [22] Boglietti, A., Cavagnino, A., and Staton, D. A., 2004, "TEFC Induction Motors Thermal Models: A Parameter Sensitivity Analysis," *Conference Record of the IEEE Industry Applications Conference*, 39th IAS Annual Meeting, Seattle, WA, Oct. 3–7, pp. 2469–2476.
- [23] Bennion, K., and Cousineau, J., 2012, "Sensitivity Analysis of Traction Drive Motor Cooling," *IEEE Transportation Electrification Conference and Expo (ITEC)*, Dearborn, MI, June 18–20, pp. 1–6.